Plasma Sources Science and Technology

PAPER

Magnetic nozzle efficiency in a low power inductive plasma source

Plasma Sources Sci. Technol. 28 (2019) 105019 (18pp) https://doi.org/10.1088/1361-6595/ab2d7d

Magnetic nozzle efficiency in a low power inductive plasma source

T A Collard and B A Jorns

University of Michigan, Ann Arbor, MI 48109, United States of America

E-mail: collardt@umich.edu

Received 23 February 2019, revised 4 June 2019
Accepted for publication 27 June 2019
Published 29 October 2019

Abstract

The nozzle efficiency and performance of a magnetic nozzle operating at low power (<200 W) are experimentally and analytically characterized. A suite of diagnostics including Langmuir probes, emissive probes, Faraday probes, and laser induced fluorescence are employed to map the spatial distribution of the plasma properties in the near-field of a nozzle operated with xenon and peak magnetic field strengths ranging from 100 to 600 G. The nozzle efficiency is found to be <10% with plasma thrust contributions <120 μN and specific impulse <35 s. These performance measurements are compared with predictions from quasi-1D idealized nozzle theory and found to be 50%–70% of the model predictions. It is shown that the reason for this discrepancy stems from the fact that the underlying assumption of the idealized model—that ions are sonic at the throat of the nozzle—is violated at low power operation. By correcting for the shifting location of the sonic transition point, the model and experiment are made to agree. The physical mechanism by which the sonic line moves with respect to the nozzle geometry is attributed to non-ideal behavior at low power. In particular, it is posited that the low ionization fraction at these low operational powers gives rise to neutral-collisional effects in the near-field of the device that can impede ion acceleration. The roles of ionization, enhanced electron resistivity, and charge exchange collisions are all examined. It is found that the ion sonic transition location is most correlated with the ratio of the charge exchange mean free path to the characteristic electrostatic acceleration length giving rise to an effective drag term on the ions.

Keywords: magnetic nozzle, electric propulsion, low temperature plasma, Detachment

1. Introduction

The increasing demand for new forms of in-space propulsion for small spacecraft has given rise in the past two decades to a growing interest in low power (<200 W) magnetic nozzle thrusters [1–16]. This interest stems largely from the number of advantages magnetic nozzles, a form of electric propulsion that employs a diverging magnetic field to accelerate a heated plasma, can offer compared to state-of-the-art technology. Due to the absence of a plasma-wetted electrode, these devices can have a longer lifetime compared to other forms of electric propulsion. They can operate on a wider range of propellants more easily stored for small spacecraft [17–22]. From a systems perspective, magnetic nozzles can be simpler than state-of-the-art thrusters (e.g. Hall effect and ion thrusters) as they do not require a separate, dedicated neutralizing electron source. Despite these apparent advantages, the demonstrated performance of state-of-the-art magnetic nozzles to date has been low: ~8% total efficiency at ~2 kW [2] with decreasing total efficiency observed at lower power. This low performance has limited the viability of magnetic nozzle electric propulsion as an alternative to more mature forms of electric thruster technology. The Hall effect thruster, for example, exhibits ⩾65% total efficiency when operating at >2 kW power levels [23].

In an effort to explain and potentially improve the low performance of magnetic nozzles, a number of previous analytical and numerical investigations have focused on developing models for their performance scaling [7, 8, 10, 24]. These models have shown that the low overall device performance largely can be attributed to high ion costs and radial wall losses. Subsequent development efforts (see [9, 12, 25]) have focused on exploring new confinement techniques and methods for ionizing the plasma. Yet, while these

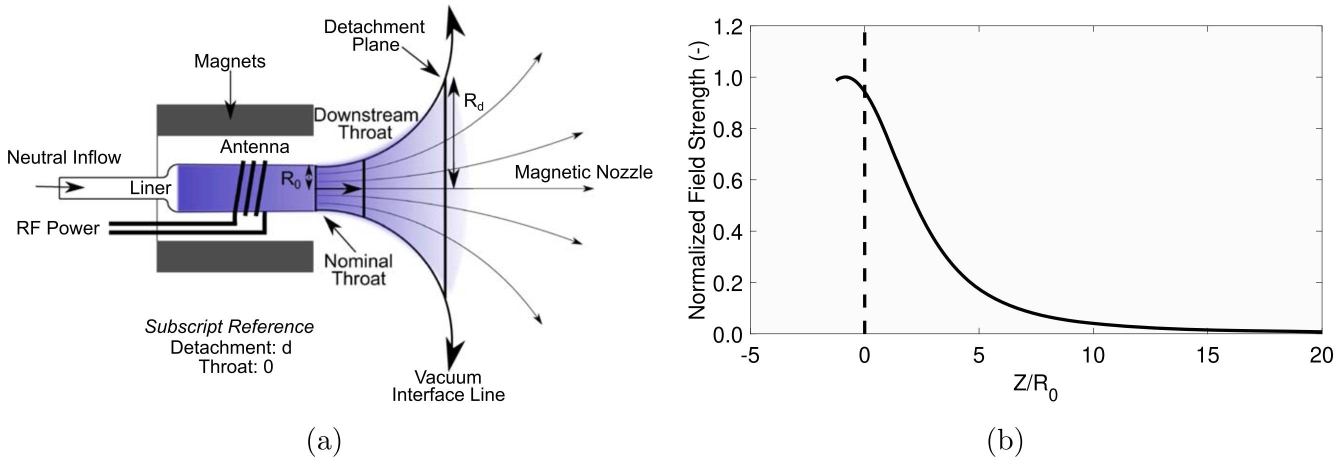

Figure 1. (a) A notional magnetic nozzle thruster. The subscripts denote key locations in the plasma. (b) The normalized magnitude of the centerline magnetic field as a function of axial position (solid curve) with the source exit plane marked (dashed line).

first-principles models have been successful in illustrating the challenges with nozzles at mid- to high-power operation ($\geqslant$200 W), the predicted performance from these models in many cases has not matched measured values at lower powers [10, 16]. This suggests that there may be other effects, beyond the two dominant ones cited above, that adversely impact magnetic nozzle performance at low power. For example, Correyero *et al* [16] were able to match measured ion acceleration and the acceleration predicted by a quasi-1D kinetic model of a low-power electron-cyclotron resonance thruster, but noted that the ion sonic condition did not coincide with the location of peak magnetic field—the location traditionally defined as the nozzle throat. Correyero *et al* posit that this downstream movement of the throat is due to diffusion and/or ionization processes, but note that their simulation work does not yet include these processes [16]. In parallel, the potential role of neutral collisions in the near-field plume at low operating powers has been explored as a potential adverse mechanism; indeed, as was shown in [12], the ionization fractions at low power can be less than 10%, thus giving rise to a large fraction of neutrals. Most models to date, however, have neglected the role of this population [3, 5, 7, 10, 24] and its impact on nozzle performance is unclear. Given the fact that low power operation is of particular interest for the new paradigm of microsats where available power on orbit is limited [26], there is a pressing need to understand and mitigate low power effects like these. To this end, the goal of this paper is to quantify and explain the discrepancies in the predictions from standard magnetic nozzle models and actual nozzle performance when operating at low power. In particular, we focus on the nozzle efficiency—the ability of the nozzle to convert thermal energy to directed kinetic energy—in a low-power, inductively-coupled test article.

This paper is organized in the following way. In section 2, we review quasi-1D analysis as applied to magnetic nozzles and derive explicit forms for the efficiency and performance terms In section 3, we describe an experimental inductively-coupled magnetic nozzle source and the diagnostics we employed to measure its plasma properties. These spatial plasma measurements and the inferred nozzle performance characteristics are presented in section 4 and compared to predictions from existing magnetic nozzle models. Finally, in section 5, we discuss the discrepancies between our measurements at low power and model predictions, and propose a possible explanation related to the low ionization fraction (the ratio of plasma density and neutral density) that these devices exhibit at low power.

2. Theoretical description of nozzle efficiency

In this work we examine the diverging part of the magnetic nozzle, i.e. the region where the plasma thermal energy is converted into directed kinetic energy. In order to quantify the discrepancy between model predictions and observed performance in this region we focus on one key parameter: the nozzle efficiency. In this section, we introduce a definition for this parameter that can be measured directly and predicted using an idealized standard model for this efficiency. This latter analysis draws from a number of previous studies on nozzle dynamics [3–6, 8, 10, 24].

2.1. Geometry

Figure 1 shows the canonical, axisymmetric geometry of a magnetic nozzle thruster we employ for this analysis. The 'upstream' region in this figure is characterized by a gas inlet, a confining liner, and concentric magnets. The plasma is created here, and electrons are heated by interactions with the applied RF field. This heated plasma transits through the 'throat,' typically assumed to be coincident with the location of peak magnetic field magnitude. Downstream of the throat, the magnetic field lines diverge and the magnitude of the field decreases. In the idealized case, electrons follow the diverging magnetic field lines and expand. The resulting pressure gradients give rise to diamagnetic currents that interact with the thruster magnets to generate a net force on the thruster [4, 6, 27–29]. In practice, the diverging magnetic field lines ultimately turn back onto themselves, and if unchecked, the plasma also will follow these lines and be re-directed back to the nozzle. It is necessary for net thrust generation that the plasma 'detach' from the field lines (denoted as the detachment plane in figure 1) at some point downstream. The problem of how and where detachment occurs is an on-going subject of research [3–6, 24, 30–34], though a number of empirical and semi-analytical criteria have been proposed. We reserve a discussion of these for later.

Functionally, although thrust generation happens through the mechanisms of plasma pressure and diamagnetic currents, magnetic nozzles can also be analyzed through the lens of conventional quasi-1D nozzle theory [8, 10, 35]. In this context, the momentum exchange in the nozzle is viewed from the perspective of the heavier species—the ions. Though these are too massive to be magnetized, the ions do experience electrostatic acceleration from the potential gradients that result from the expansion of the electrons. This process draws direct parallels to conventional gasdynamic nozzles in which the thermal energy of the propellant (as stored in the electrons) is converted to directed acceleration of the propellant (as represented by the ions). In this case, the ions are accelerated until the detachment plane, which can be equated to the effective exit plane of a conventional nozzle. Significantly, the analogy carries beyond a qualitative analysis, and it has been shown that these nozzles lend themselves to quasi-1D nozzle expansion theory (see [36]) in which the thrust is related to the cross-section of the nozzle. This is the formalism and physical interpretation we apply here in which we discuss the expansion and acceleration of the exhaust through the throat with cross-sectional area, A_0, and the exit plane with cross-sectional area, A_d. In the absence of walls, the radius of the nozzle geometry at each location (see figure 1) is defined from the centerline to the vacuum interface line—the magnetic field line that grazes the edge of the source at the exit plane.

2.2. Measurable expression for nozzle efficiency

For our analysis, we first begin by introducing a generalized definition of overall thruster efficiency, i.e. directed exhaust power to input power (see [37]):

$$\eta = \frac{T^2}{2\dot{m}P_0}, \tag{1}$$

where $\dot{m}$ denotes the flow rate of the propellant, P_0 is the input power to the system, and T is the thrust. For magnetic nozzles, this efficiency is a product of a number of contributions, $\eta = \eta_{\mathrm{rf}}\eta_{\mathrm{m}}\eta_{\mathrm{loss}}\eta_{\mathrm{noz}}$, where η_{rf} denotes the efficiency of conversion of RF input power to thermal energy inside the plasma source, η_{m} is the mass utilization efficiency, η_{loss} is the efficiency of the source dictated by losses to the source walls, and η_{noz} is the efficiency of conversion of thermal energy passing through the nozzle throat to energy employed for thrust [7, 10, 24, 34, 38]. The first three components of the efficiency are 'source-related,' i.e. they dictate how well the RF source ionizes and couples thermal energy into the propellant before it is accelerated through the nozzle [7, 10, 24, 34, 38]. Our analysis, however, focuses on the downstream contributions to the efficiency from the nozzle, which can be written as

$$\eta_{\mathrm{noz}} = \frac{T^2}{2\dot{m}_{\mathrm{ion}}P_{\mathrm{noz}}}, \tag{2}$$

where P_{noz} is the power entering the nozzle from the source region, $\dot{m}_{\mathrm{ion}}$ is the mass flow rate of ions, and we have assumed that the plasma is singly ionized. This latter assumption is plausible given the typically low electron temperatures in these devices [10, 12, 25, 34]. Physically, this expression represents the fraction of thermal energy flowing into the nozzle that is converted to useful directed kinetic energy for thrust.

We can find explicit expressions in terms of plasma plume properties for both the inlet energy to the nozzle as well as the thrust by employing quasi-1D nozzle analysis to the geometry shown in figure 1. For the thrust, we apply a control volume analysis coupled with the assumption that the plasma has a quasi-1D expansion (the plasma properties are approximately constant across each axial slice) to find

$$T = \dot{m}_{\mathrm{ion}}u_d + \bar{p}_e A_d, \tag{3}$$

where A_d is defined as before, $\bar{p}_e$ is the average plasma pressure across the nozzle section at the detachment location, and u_d is the axial component of ion velocity at the detachment location. To evaluate the power flow into the nozzle in (2), we again consider a quasi-1D flow and follow previous work in assuming the electron pressure expansion in the nozzle is governed by polytropic cooling [9, 39–43]. We thus can write (see appendix)

$$P_{\mathrm{noz}} = \left[\frac{1}{2}m_i u_0^2 + \frac{5}{2}qT_{e,0} + \frac{3}{2}qT_{e,0}\left(\frac{5/3-\gamma}{\gamma-1}\right) + q\epsilon_c\right] \times n_{e,0}u_0A_0, \tag{4}$$

where m_i is the ion mass, ϵ_c is the ion cost in eV, $n_{e,0}$ is the average density in the throat, $T_{e,0}$ is the electron temperature in the throat, A_0 is the cross-sectional area of the throat, q is fundamental charge, u_0 is the ion drift velocity in the throat, and γ is the polytropic index. This expression represents the power flowing into the nozzle with contributions from ion kinetic energy (first term), electron pressure (second term), heat conduction (third term), and ion creation losses (last term). This last term historically has been dominant in magnetic nozzle sources [9, 10, 34] and represents an effective 'frozen flow' loss for the creation and maintenance of the plasma. The 'frozen flow' losses depend on the ionization and excitation states of the ions and the electron temperature (see appendix for further discussion).

Armed with (2)–(4), we thus have the ability to evaluate the nozzle efficiency experimentally provided we know the location of the detachment plane and have measurements of key plasma properties in this plane. Given the challenges with measuring the low thrusts generated from these devices directly, this type of assessment of performance from plasma measurements has formed the basis for a significant fraction of the studies performed on these devices to date [2, 34, 40, 41, 44].

2.3. Model for nozzle efficiency

There have a been a number of modeling efforts on magnetic nozzles to date—ranging from analytical [8, 10, 35, 38] to 2D numerical codes [3–7, 24, 39]—to predict key performance parameters like the the overall efficiency. In order to provide representative results for the predictions of these models in comparison to our experimental measurements for a low power system, we consider a model informed by the interpretation of the magnetic nozzle in terms of a traditional nozzle analysis. In particular, it is possible to relate the overall performance and efficiency to the inlet conditions at the throat and the expansion ratio of the nozzle (A_d/A_0). The form of this relation varies depending on the assumptions made concerning the expansion process. For our work, we leverage insight from previous analytical studies [3–10, 24, 30, 31, 34, 40] to make four key assumptions:

- The neutral species can be neglected
- The ions are cold
- The ions are sonic at the throat (location of peak magnitude field), i.e. $M = u_0/c_s = 1$, where M denotes the ion Mach number and c_s is the local Bohm speed ($c_s = \sqrt{\gamma q T_{e,0}/m_i}$)
- The plasma expansion is polytropic and governed by an equation of state $T_e(n_e)^{1-\gamma} =$ constant, where $1 \leqslant \gamma \leqslant 5/3$.

This last assumption of polytropic cooling has been supported by a number of experiments that have been performed to date on magnetic nozzles. These have shown empirical values between 1.1 and 1.4 [9, 42, 43]. Physically, the value of the polytropic index for xenon is bounded by two limits, representing infinite heat conduction along field lines from the source (isothermal, $\gamma = 1$) and no electron thermal conduction (adiabatic, $\gamma = 5/3$ for noble gases). We choose to leave the model with an arbitrary, but constant polytropic index as we have the ability to measure it directly in our system (section 4).

Using the above assumptions we can find an expression for the theoretical nozzle efficiency:

$$\eta_{\mathrm{noz},t} = \frac{M^2 \gamma T_{e,d}}{[5 + \gamma + 3\left(\frac{5/3-\gamma}{\gamma-1}\right) + \frac{2\epsilon_c}{T_{e,0}}]T_{e,0}} \eta_{\mathrm{div}}, \tag{5}$$

where $M = u_d\big/\sqrt{\gamma q T_{e,d}/m_i}$ denotes the ion Mach number at the detachment plane and η_{div} is a divergence efficiency that corrects for the 2D nature of the plume expansion. We can find this latter parameter by geometric arguments or direct measurements of the plume expansion. Conversely, we can find the Mach number at the detachment plane provided we know the detachment location and its associated cross-sectional area. In this case, the Mach number is related to the expansion ratio and inlet ion velocity in the following way:

$$T_{e,d} = T_{e,0}\left(\frac{u_0 A_0}{u_d A_d}\right)^{\gamma-1} \tag{6}$$

$$u_d^2 = u_0^2 + \frac{2\gamma q m_i T_{e,0}}{\gamma - 1}\left[1 - \left(\frac{u_0 A_0}{u_d A_d}\right)^{\gamma-1}\right]. \tag{7}$$

These stem from the equation of state for electron energy and ion continuity under the assumption of a collisionless plasma. Provided that the inlet conditions to the nozzle and the expansion ratio are known (5)–(7), allow for the evaluation of the nozzle efficiency and by extension the thrust via (3). Physically, these results show that as the expansion ratio increases, the plasma can expand more leading to a greater acceleration of the plasma. This is consistent with traditional de Laval nozzle theory [36].

2.4. Location of detachment plane

Both the experimental and analytical expressions outlined in the preceding require an estimate for the detachment point of the plasma from the magnetic field. While there are a number of proposed theories for this location, both analytical and semi-empirical [3–6, 24, 30–34], to date there has not been a consensus about its location. We introduce for this study an experimentally-driven criterion that we apply both for the experimental evaluation of performance and the analytical model. We conjecture that when the ions have stopped accelerating, i.e. the ion velocity as measured on the nozzle centerline is constant, the plasma has effectively become detached from the nozzle. This criterion stems from the assumption that if the ion velocity is constant, the ions are no longer being accelerated by the nozzle dynamics. As we discuss in the following section, we are able to infer the transition to this point by employing a combination of ion velocimetry and current density diagnostics.

3. Experimental apparatus

3.1. Plasma source and vacuum chamber

To quantify the performance of the experimental low-power magnetic nozzle device using the above generalized performance framework requires initial and boundary conditions that must be informed by experimental measurements. For our investigation we employed a radiofrequency (RF) plasma source 13 cm in diameter with an integrated 2.5 cm diameter by 1.9 cm long ($R_0 = 12.5$ cm, $L_0 = 1.9$ cm) monolithic quartz plasma liner (figure 2). Neutral xenon propellant was injected into the source tube through a central hole in the back of the quartz liner with a fixed flow rate of 3 mg s^{-1}. The neutral propellant was excited by a 3-turn solenoidal antenna wrapped around the quartz liner. The antenna was constructed of 3 mm hollow copper tubing enabling water cooling to minimize impedance variations due to thermal loading. It was connected to a transmission line comprised of a bi-directional coupler, an L-type automatic matching network, and an RF

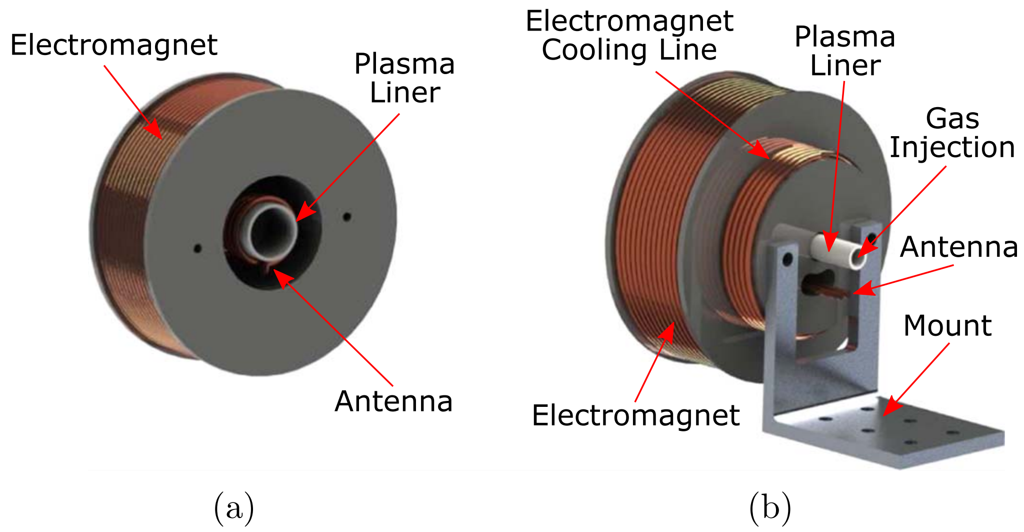

Figure 2. A (a) front and (b) rear isometric view of an as-built 3D model of the plasma source. Note that the front section of the Faraday shield is removed to allow for the internal components to be viewed. This shield is installed for the experiments discussed herein.

amplifier operating at 13.56 MHz. The directional coupler provided *in situ* forward and reflected power telemetry while the automatic matching network improved power coupling by reducing the reflected power, typically to below 20% of the forward power.

The converging-diverging magnetic nozzle was produced by an electromagnet constructed of 10 AWG square enamel coated copper magnet wire. The current through the electromagnet was controlled to produce peak nozzle throat strengths up to 900 G. To mitigate thermal loading and maintain steady-state operating temperatures below the maximum 240 °C wire threshold the electromagnet spool was water cooled.

The integrated plasma source was mounted on support structure within the Junior Test Facility at the University of Michigan. Junior is a 3 m long by 1 m diameter stainless steel clad vacuum chamber backed by a combination of rotary, turbomolecular, and cryogenic pumps. This facility was selected due to the small size of the device (13 cm in diameter, overall) to minimize plasma-swall interactions. The effective pumping speed for the experiments described herein was $\sim$15 000 l s^{-1} on xenon. With this pumping capacity the base pressure of the Junior facility is $\sim 1 \times 10^{-8}$ Torr xenon and the background pressure was $\sim 4 \times 10^{-5}$ Torr xenon during full source operation.

3.2. Diagnostics

To fully characterize our nozzle source and the plasma parameters of interest (section 2), we employed probes to measure the magnetic field, ion velocity, neutral density, plasma density, electron temperature, plasma potential, and ion current density. The axial and radial ion velocity profiles were measured using a 2D time-averaged laser induced fluorescence (LIF) setup [45] with an effective spatial resolution of $\sim$1 mm. The non-resonant LIF scheme we used targeted the $5d^2F_{7/2}$ to $6p^2D^0_{5/2}$ metastable line of xenon ions and yielded an ion velocity distribution function (IVDF). The plasma parameters were measured with a suite of electrostatic probes, including an unguarded nude Faraday probe (ion saturation current), a double Langmuir probe (plasma density and electron temperature), and an emissive probe (plasma potential). To accommodate the small size of the plasma source the tungsten collection electrodes of the Faraday probe and double Langmuir probe were 1.6 mm and 0.5 mm in diameter, respectively. Due to the small characteristic dimension of the probes and the sparse plasma density the measurements were corrected for sheath expansion effects following Sheridan's method [46]. This sheath expansion correction was included in both the Faraday and double Langmuir probe analyses. The thoriated tungsten hairpin loop emissive probe was operated in the limit of high emission, with measurements in both the cold and saturated emission states allowing for estimation of the plasma potential by including the electron temperature factor correction of the hot floating potential [47]. The magnetic field topography was measured with a Lakeshore Model 460 3-axis Gaussmeter. A Stabil Ion Gauge with an integrated Pitot tube measured the neutral pressure throughout the plume, allowing for estimation of the neutral density.

To preserve optical alignment the plasma source was attached to a pair of translation stages while the laser optics were fixed. The plasma source then was moved to interrogate multiple points within the plume. This LIF setup is shown in figure 3. For all other probes the plasma source was mounted at a fixed location within the vacuum chamber and the diagnostics were translated via the motion stages.

4. Results

In this section we present the measurements of the plasma properties necessary to evaluate the measured and model predictions for nozzle performance. These data were taken with the nozzle operating at $\sim$170 W combined deposited power into the transmission line and plasma source and

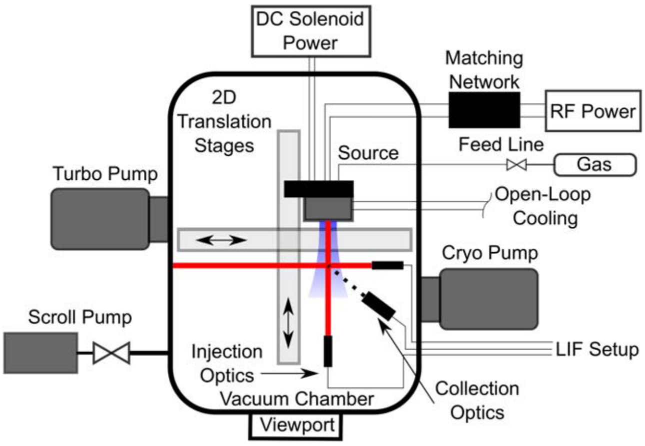

Figure 3. The experimental setup used to measure the spatial evolution of the ion velocity distribution throughout the expanding magnetic nozzle using LIF.

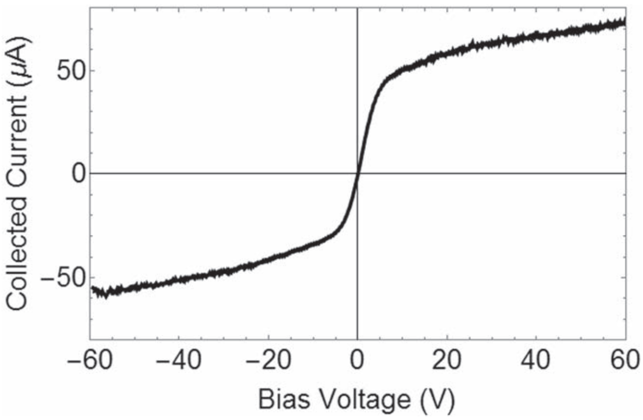

Figure 4. A characteristic *I–V* trace measured with the double Langmuir probe. This specific trace was measured at the centerline, exit plane of the source operating with ~170 W input power, 3 mg s^{-1} of xenon, and a field strength of 300 G.

3 mg s^{-1} xenon propellant flow rate. We took measurements for magnetic field strengths ranging from 100 to 600 G at 100 G intervals. These operating conditions were selected due to the source stability and repeatability over a wide range of magnetic field conditions—the source was operated for $\geqslant$12 h per run with <1% change in the source telemetry and exit plane plasma measurements, and between each run the telemetry and exit plane measurements matched within 1% upon restart. The ability to tune the magnetic field strength while keeping the propellant flow rate and input power constant assists in isolating the underlying mechanisms impacting performance.

4.1. Plasma properties

4.1.1. Plume properties. We measured plasma density and electron temperature by using a double Langmuir probe and fitting functions to different parts of the *IV* curve, following the procedures outlined by Brockhaus *et al* [48]. A sample raw trace—for the 300 G operating condition and at the centerline, exit plane location—is shown in figure 4. This analysis relies on the assumption of a Maxwellian plasma. Following this prescription, we were able to measure these plasma parameters over a range of positions. In figure 5 we show contour maps of the measured plasma density, plasma potential, and electron temperature in the nozzle plume. The electron temperature map in figure 5(a) shows cooling as the plasma expands downstream. This indicates that the plasma is not isothermal and is losing thermal energy. In turn, this cooling is correlated with the spatial distribution of the plasma potential, which figure 5(b) shows is highest at the nozzle inlet and decreases with distance from this plane. The electrostatic field in the plume that results from this potential structure is the mechanism for accelerating ions. The plasma density plot (figure 5(c)) shows the evident expansion of the plasma in the axial and radial directions with the highest density concentrated on centerline at the throat. This is consistent with the plasma pressure, as represented by the electron pressure, decreasing as it expands. The convolution of the ion acceleration and the density profile is captured in the axial ion current density plot in figure 5(d). However, there is a notable feature in the plasma density and current density profiles: for slices at constant axial location beyond the $(Z/R_0) = 1$ plane, the plasma density exhibits a radially non-monotonic dependence. This is characterized by an effective 'clustering' near the vacuum interface line. This type of structure has been observed before [25] and may be explained in part by a combination of spatially non-uniform heating within the plasma liner [49, 50] and the presence of a corresponding well in plasma potential along this boundary (figure 5(b)). This potential well structure has been noted in a number of magnetically confined plasmas [34, 51–53] and can be interpreted as the consequence of charge separation that results from ions with sufficient transverse energy overshooting the attached electron fluid. The potential well forms to counter this finite transverse ion inertia and deflect the ion streamlines back toward the field-aligned electron streamlines [34, 51].

4.1.2. Ion acceleration. Taken together, the plasma measurements in figure 5 show that the conditions are appropriate for electrostatic ion acceleration. We measured this acceleration directly in the near-field with the LIF system by characterizing the axial and radial IVDFs simultaneously (see figure 6(a)). The mean velocity in each direction is calculated by taking the moment of these distributions after applying a sums-of-gaussians fit. Due to the presence of the magnetic nozzle, we assessed the potential impact of Zeeman splitting on our results. Following the approaches of Jorns *et al* [54] and Huang *et al* [55], and assuming that the ion velocity distribution is Maxwellian, we estimate that Zeeman splitting adds $\leqslant$5% to the uncertainty in the ion velocity measurements at the exit plane, in both the cross-field and field-aligned directions. Due to the rapid decay in the magnetic field strength with increasing distance from the exit plane, the uncertainty due to Zeeman splitting decreases downstream. This low uncertainty contribution allows us to neglect this effect in our analysis of the results. The resulting

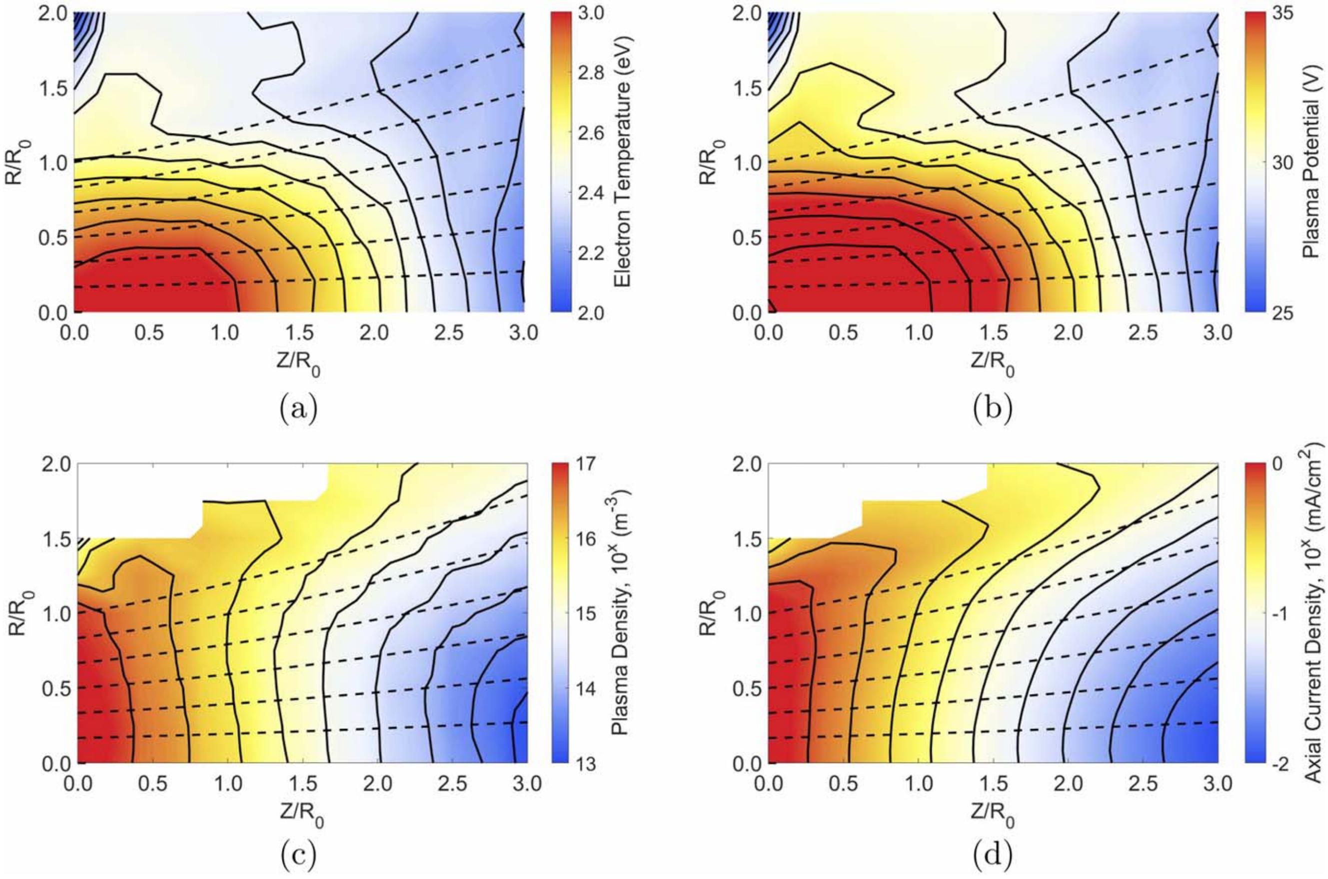

Figure 5. (a) A spatial map of the electron temperature, (b) plasma potential, (c) plasma density and (d) axial ion current density (contour and solid curves) with an overlay of the magnetic nozzle field lines (dashed curves) for the 400 G, ~170 W net deposited power, and 3 mg s^{-1} xenon propellant flow rate operating condition. Note the potential well near the vacuum interface line and that the axial position is referenced to the throat location.

vector map exhibits a subsonic ion speed at the source exit plane ($c_s \sim 1.5$ km s^{-1} for this 400 G condition) and large radial velocity components throughout the plume. The error in these measurements is estimated as the 95% confidence interval after bootstrapping the IVDFs 10 000 times; the largest error is at $(Z/R_0, R/R_0) = (5/4, 3/2)$mm with $\pm 12\%$ error in speed and $\pm 4°$ in angle. The trajectories of the ions are consistent with our measurements of the plasma potential in figure 5. Indeed, following these contours, it is evident that the ion trajectories appear to be driven by electrostatic acceleration resulting from the potential structure. This is consistent with our physical interpretation of the nozzle dynamics outlined in section 3. Moreover, we note that our results are consistent with previous nozzle studies in two signficant ways. First, as shown in figure 6(b), the ions are in fact accelerated, albeit not prodigiously, in the axial direction as they transit downstream. This is an indication that the ions are gaining directed kinetic energy as they transit the nozzle. Second, the ions appear to exhibit an 'outward separation' in so much as their trajectories diverge more quickly than the nozzle streamlines. This type of ion motion has been seen both experimentally [34] and predicted numerically [5].

Due to low signal-to-noise ratio in the downstream region where the plasma becomes more sparse, we were only able to map the ion trajectories using LIF in the region shown in figure 6. To supplement the near-field data and provide a more complete depiction of the ion dynamics, we also mapped the ion current density in the far-field (see figure 5(d)). This spatial map, like all the electrostatic probe maps, extends from the near-field into the plume far-field. The overlapping of the ion current density map with the LIF measurements allows for the inference of the far-field ion velocity when coupled with the plasma density measurements, assuming that the plasma is singly ionized ($j = qn_{eu}$). This map reveals a new detail for the ion trajectories: as shown in figure 6(c) the centerline ion velocity plateaus within $(Z/R_0) \sim 5$. Consistent with our definition in section 2, thus we are able to empirically designate this plane as the detachment location.

4.1.3. Mach number. In figure 6(d) we show a plot of the calculated ion Mach number. This result reveals a notable feature that is inconsistent with the physical assumptions we outlined for the model described in section 2: it is evident that at the inlet plane of the nozzle, which is characterized by the peak magnetic field magnitude, the ions have not become sonic. Instead, the sonic transition occurs farther downstream at location $(Z/R_0) \sim 0.5$, on average across the nozzle. This result is consistent with recent work that has been performed on a low power electron-cyclotron resonance thruster [16] and

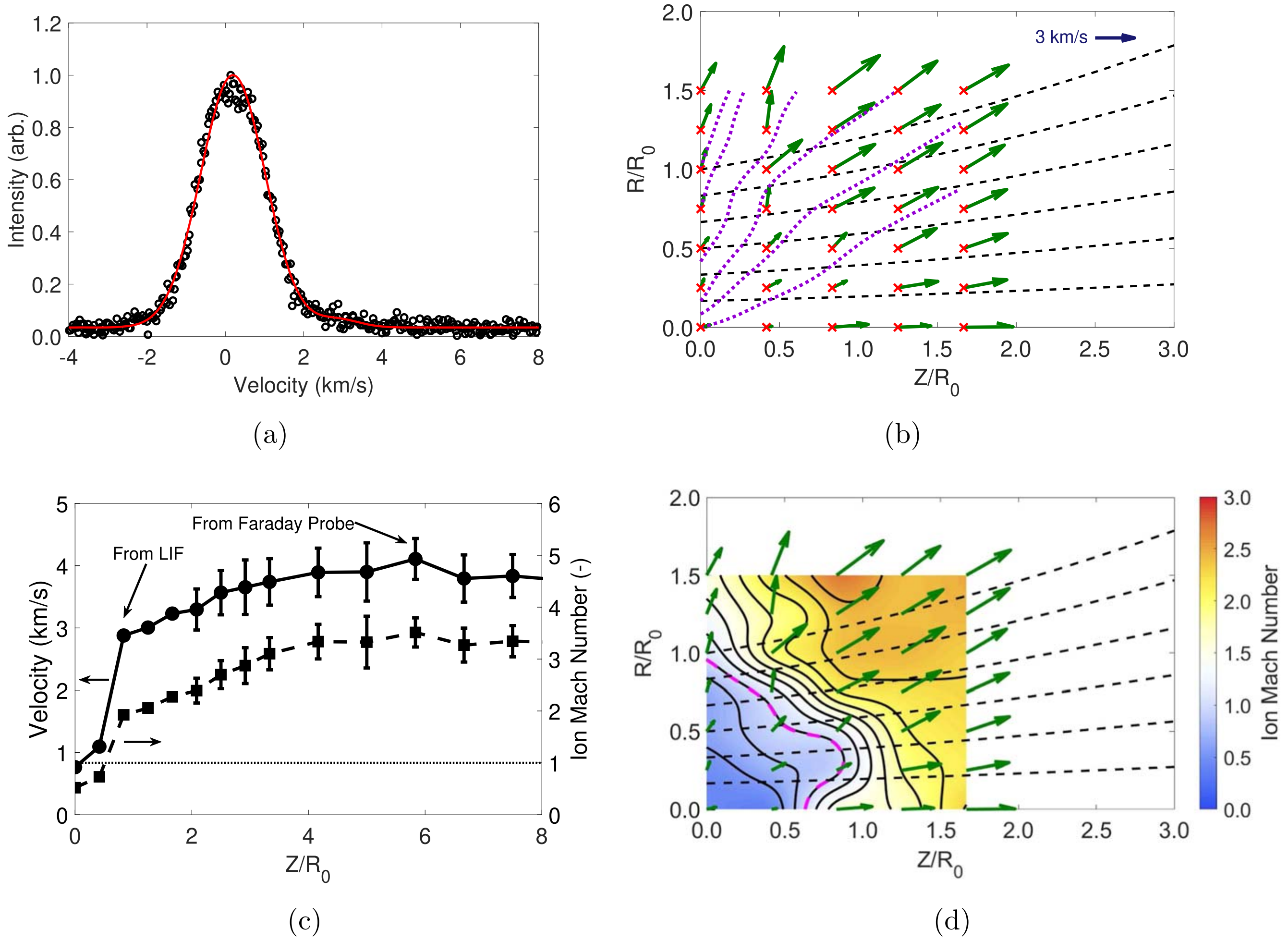

Figure 6. (a) An example axial IVDF at $(Z/R_0, R/R_0) = (0, 1/4)$ with a sums-of-Gaussian fit (solid curves) to the raw data (circles). (b) The resulting ion velocity vectors (arrows) and corresponding ion streamlines (dotted curves). (c) The mean axial ion velocity on centerline. (d) The inferred local ion Mach number (contour and solid curves) with an overlay of the magnetic nozzle field lines (dashed curves). All data is taken from the 400 G, ~170 W net deposited power, and 3 mg s^{-1} xenon propellant flow rate operating condition. Note that the measurement locations are indicated by an 'x' and that the axial position is referenced to the throat location.

seems to be evidence that the idealized nozzle expansion may have some limitations in describing this low power regime of operation. We revisit this in the following section.

4.1.4. Polytropic cooling. With the plasma measurements from the preceding sections, we have nearly all of the information required to evaluate both the experimental and analytical predictions for nozzle conversion efficiency. The remaining key element is the polytropic cooling index. We can estimate this value by noting that $\mathrm{d}\phi/\mathrm{d}T_e = \gamma/(\gamma - 1)$ and using linear regression of the plasma potential versus electron temperature [40, 42]. The resulting best fit linear regression to the data along centerline is shown in figure 7(a) for the six magnetic field settings that we investigated in this work. The error is estimated by using the lines fit to the extremes of the data and its associated error, resulting in the steepest and shallowest line slopes (see figure 7(b)). For comparison, we also show the polytropic index for adiabatic and isothermal cooling. In all six cases, it is evident that $\gamma \sim 1.1$, which is within the range of measured values for electric propulsion devices operating on xenon [9, 41–43], and between the adiabatic ($\gamma = 5/3$) and isothermal ($\gamma = 1$) limits.

Summarizing the above results, we see that this low power nozzle does exhibit the type of behavior we expect for these devices. Electron thermal energy evidently is converted to ion kinetic energy with the magnetic field acting as a mediating factor. This acceleration then occurs until a discrete downstream 'exit plane.' In the next section, we apply the formalism outlined in section 2 to quantify the efficacy of this nozzle conversion and compare it to the analytical predictions.

4.2. Nozzle performance

4.2.1. Efficiency. Leveraging the results from the previous section, we can employ the formulations from section 2—equations (2)–(5)—to evaluate the nozzle efficiency. To this end, we estimated the location of the detachment plane as the location where the ion velocity plateaus, as inferred from the Faraday probe, yielding A_d. We estimated the axial component of the ion velocity at this exit plane from the

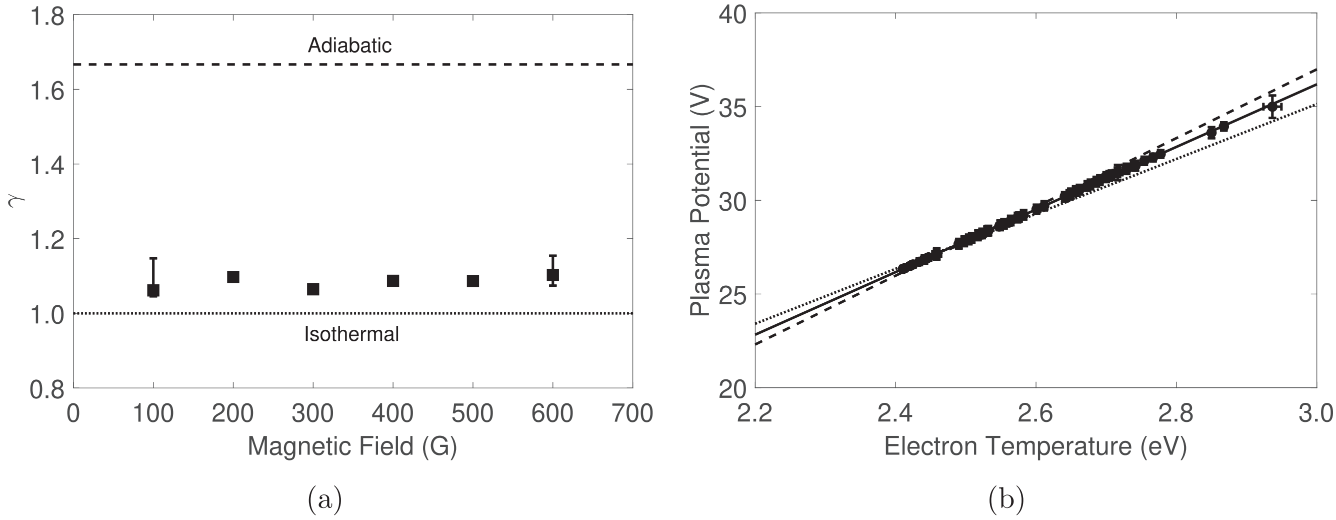

Figure 7. (a) The value of the polytropic index inferred using linear regression of the plasma potential versus the electron temperature for the source operating conditions (squares). Note that value of the polytropic index is bounded by the adiabatic ($\gamma = 5/3$, dashed line) and isothermal ($\gamma = 1$, dotted line) limits. (b) The measured centerline plasma potential versus the electron temperature (circles) for the 400 G operating condition and the best-fit regression line (solid line). The error in the polytropic index is calculated by using the lines fit to the data, and its associated error, such that the minimum and maximum slopes are obtained (dashed and dotted lines). Across all magnetic fields the device is operated at ~170 W net deposited power and 3 mg s^{-1} xenon propellant flow rate.

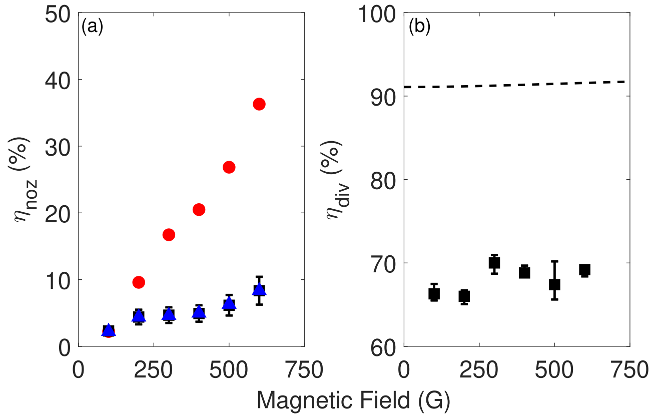

Figure 8. (a) The inferred nozzle efficiency from measurements of the plasma source (squares) compared to the efficiency predicted by the ideal model (circles) and the model using the downstream throat properties (triangles). (b) The divergence efficiency of the plasma source (squares) compared to the divergence efficiency of a fully attached, ideal nozzle that detaches at the same location. In all magnetic field conditions the source is operated with a net deposited power of ~170 W and propellant flow rate of 3 mg s^{-1} xenon.

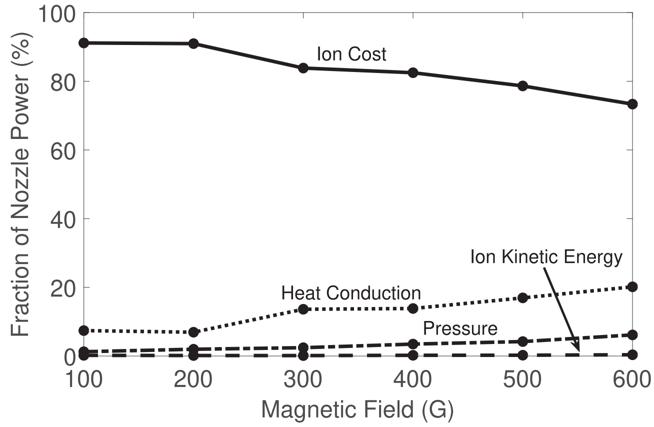

Figure 9. The fraction of all modes to the total power flowing into the nozzle. Note that at each magnetic field strength the net deposited power is ~170 W and xenon propellant flow rate is 3 mg s^{-1}.

Faraday probe data, yielding a value for u_d. We approximated the ion flow rate by using the measured density (double Langmuir probe), ion velocity (LIF), and source geometry at the throat ($\dot{m}_{\mathrm{ion}} = m_i n_{e,0} u_0 A_0$). We determined the electron temperature at the throat using the double Langmuir probe measurements to yield $T_{e,0}$ and we used the polytropic index of ~1.1 from figure 7. And finally, we estimated the ion energy cost using the analysis outlined in Lieberman and Lichtenberg [56] to yield ϵ_c. Combining these measurements and inferred values at the throat yielded a calculated power flowing into the nozzle and an estimate for thrust. With these values, we ultimately were able to use (2)–(4) to generate a plot of the nozzle efficiency, as shown in figure 8(a).

This result shows that the nozzle contribution to the overall efficiency is markedly low, <10%. In other words, this low power nozzle is only capable of converting 10% of the available energy at the inlet into directed exhaust. The major driver for this loss in efficiency is illustrated by looking at the different contributions to the nozzle power in (4), shown in figure 9. It is evident from this figure that the largest term is the ion cost, scaling with ϵ_c. This finding is consistent with previous works [7, 8, 10, 24] and underscores the dominant role of frozen flow losses associated with ion production. For illustative purposes and to capture the magnitude of the impact of the ion cost term, consider the nozzle efficiency if the frozen flow losses could be neglected (η'_{noz}); for the 400 G

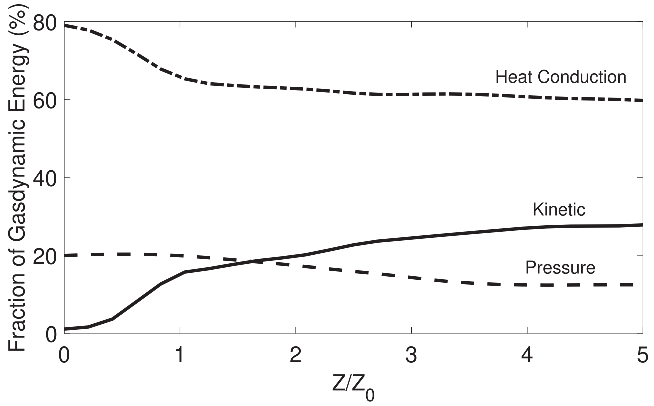

Figure 10. The axial evolution of the fraction of the total gasdynamic energy entering the nozzle—the first three terms in (figure 4—for the 400 G, ~170 W, 3 mg s^{-1} of xenon operating condition.

operating condition $\eta'_{\mathrm{noz}} \sim 24\%$. This is ~5× higher than the actual nozzle efficiency, demonstrating the impact of the frozen flow losses on the nozzle efficiency.

On the other hand, we note that the nozzle efficiency does monotonically improve with magnetic field strength. Physically, this trend is expected because our measured electron temperature at the throat increases with increasing magnetic field, and as previous work has shown, increased electron temperature can translate to improved efficiency [9, 10, 34]. We do note that the trend in electron temperature with magnetic field is not predicted by classical 0D global power balance models [56]; this power balance predicts that electron temperature decreases with increasing magnetic field strength due to the correspoding decrease in plasma diffusion to the radial walls. This discrepancy does not impact our analysis here as we focus on the downstream dynamics of the source. However, we note that there are a number of possible explanations for this result. For example, as Kinder and Kushner proposed, the increased electron temperature at higher magnetic field conditions may be explained by spatially non-uniform power deposition; a result that is numerically predicted for solenoidal antenna power coupling to a plasma in the presence of a magnetic field [49, 50].

In addition to the various energy terms entering the nozzle, we can observe the energy transfer between the gasdynamic modes throughout the nozzle by using the plasma measurements in figure 5. Figure 10 illustrates this energy transfer in the nozzle for the 400 G operating condition. From these results the pressure term decreases from ~20% to ~12% and the heat conduction decreases from ~79% to ~60%. The energy from these modes is transferred into ion kinetic energy, which increases from ~1% to ~28%. It is clear that the decrease in the pressure term is not sufficient to account for the ion kinetic energy increase. This suggests that the heat conduction is coupled with the ion kinetic energy, and the electron cooling results in a decrease in the heat conduction and a corresponding acceleration of the ions. While the energy transfer between heat conduction and ion kinetic energy is promising, Little and Choueiri [40] showed —through the lens of the Nusselt number, or the ratio of the convected heat to conducted heat—that efficiency losses may be incurred due to unrecovered electron thermal energy for devices in which the power entering the nozzle is dominated by heat conduction. The dominant energy term in our nozzle, aside from the frozen flow losses, is the heat conduction, so we next evaluate the potential efficiency penalty incurred by our nozzle by calculating the Nusselt number. For our operating conditions the Nusselt number was of the order of ~0.01 to ~0.1, which suggests that the maximum nozzle efficiency of our device may be limited to ~50%–80% due to a portion of the electron thermal energy being unrecoverable [40]. This effect is not sufficient to explain the low nozzle efficiency in figure 8(a). A Nusselt number 2–10× smaller than the values observed in our device would be required to match the measured efficiency loss, suggesting that unrecoverable electron thermal energy may be only one of several effects limiting the nozzle performance.

For comparison to these measured results, we next evaluate the analytical predictions for the nozzle efficiency. To this end, we follow the conventional approach used in the formulation in section 2, where we assign the 'throat' to be the exit of the liner. We assume an expansion ratio consistent with the detachment point measured in figure 6(d) ($A_d/A_0 = 6.7$) and that the ions are sonic at the throat. We also employ the measured electron temperature at the throat (figure 5(a)) and the polytropic index (figure 7). Also, as can be seen from (5), in order to do a comparison between the analytical nozzle efficiency and measurements, we need to take into consideration the divergence efficiency of the system. We evaluated this correction by using Faraday probe measurements in the detachment plane and the iterative path-finding method recommended by Brown *et al* [57] for use with these near-field Faraday probe measurements. As can be seen in figure 8(b), for all the magnetic field settings this yielded a divergence efficiency of $\eta_{\mathrm{div}} \approx 68\%$. Armed with this result, we are able to plot the analytical predictions for nozzle efficiency in figure 8(a). From the comparison of the model and source results, it is immediately apparent that the analytical nozzle efficiency model overpredicts the measured value for all magnetic field settings by a factor of ~5 at the highest magnetic field case (600 G). This is direct evidence that these types of idealized nozzle expansions are not representative of our actual system and underscores the point that, at low power, similar magnetic nozzles have a more nuanced behavior.

There could be a number of reasons why this discrepancy occurs, but the explanation we explore here stems from observations outlined in the previous section and informed by the work of Correyero *et al* [16]: the ions are not actually sonic at the expected throat location. Critically, one of the key assumptions underpinning the physical model has been violated. With this in mind, we can explore the validity of the analytical model if we re-define the throat to not be coincident with the location of peak magnetic field, but, in keeping with the definition of classical nozzles, where the ions become sonic—location $Z/R_0 = 0.5$, as shown in figure 6. By using this A_0 and the plasma parameters at this revised inlet plane, but preserving the same detachment location, we recover the experimentally inferred nozzle

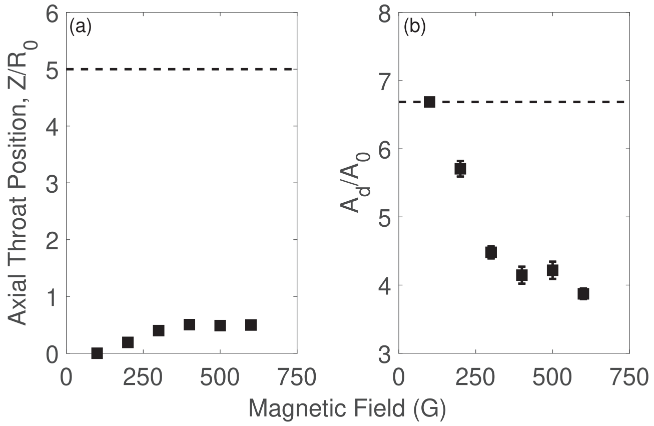

Figure 11. (a) The downstream axial location of the effective nozzle throat (squares) and the detachment plane location (dashed line). (b) The area expansion ratio of the nozzle after the throat is shifted downstream (squares) compared to the ideal nozzle expansion ration (dashed line). In all magnetic field conditions the source is operated with a net deposited power of ~170 W and propellant flow rate of 3 mg s^{-1} xenon.

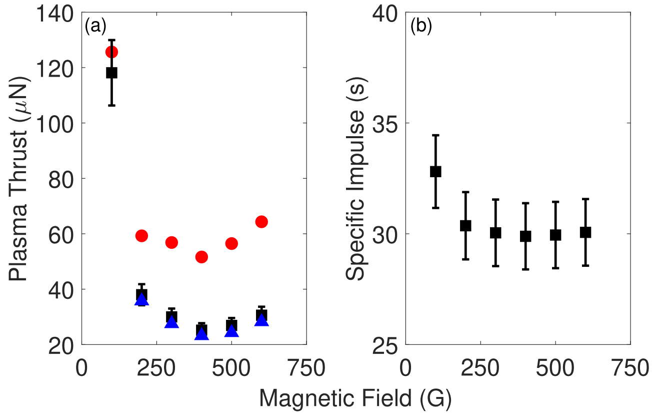

Figure 12. (a) The inferred plasma contribution to thrust from measurements of the plasma source (squares) compared to the thrust predicted by the ideal model (circles) and the model using the downstream throat properties (triangles). (b) The inferred specific impulse. In all magnetic field conditions the source is operated with a net deposited power of ~170 W and xenon propellant flow rate of 3 mg s^{-1}.

efficiency results shown in figure 8(a). This result shows that by adjusting the throat to this new location the predicted and measured efficiency are directly coincident. The physical reason for this reduced performance is that we are effectively lowering the expansion ratio by moving the nozzle throat further downstream. This translates to a lower overall expansion through the nozzle and reduced recovery of thermal energy. This is strong correlational evidence that the model is still applicable, provided we track more carefully the sonic condition, as found by Correyero *et al* [16].

Moreover, the increasing discrepancy between the model and source efficiency with increasing nozzle strength can be explained by tracking the location of the sonic condition as a function of magnetic field setting. This is shown in figure 11(a) along with the location of the exit plane inferred from the procedure outlined above. Notably, the detachment plane does not shift, but with increasing magnetic field, the location of the throat—and therefore effective area of the throat—moves downstream. As shown in figure 11(b), this translates to a lower expansion ratio with increasing magnetic field strength compared to the expansion ratio that would be assumed if we ascribed the throat simply to the source exit plane. This explains why the model and actual efficiency results diverge more with increasing magnetic field strength.

4.2.2. Thrust and specific impulse. Physically, the reason why the expected throat and actual sonic line are not coincident at this low power is not immediately apparent. Before we discuss this in the following section, however, we briefly present here an analysis of other key performance parameters that can be inferred from these measurements: the thrust and specific impulse. In the experimental plasma source the plasma contribution to thrust is calculated using (3) and is shown in figure 12(a). This thrust is compared to the plasma-generated thrust for the idealized model in section 2. For this latter calculation, we inferred thrust from the same equation but used the results from the model—equations (5)–(7) with $\gamma = 1.1$, $A_d/A_0 = 6.7$, and measurement-inferred throat parameters—to determine the various detachment plane parameters (u_d, $T_{e,d}$, $n_{e,d}$). From these results the experimental source achieves thrust that is ~50%–70% of the expected plasma thrust with a very low overall value. This is consistent with the efficiency measurements and can be explained similarly by the changing location of the throat. To calculate the specific impulse the plasma-generated thrust must be added to the cold gas thrust, which we calculate to be ~850 μN, from $F_g = (\dot{m}_p - \dot{m}_{\text{ion}}) v_g [1 + qT_g/(m_i v_g^2)]$ where $v_g = \sqrt{(5/3) qT_g/m_i}$ [10]. The neutral gas temperature is assumed to be room temperature ($T_g = 0.026$ eV). Due to the dominance of the cold gas thrust at these low power conditions the specific impulse is limited to several 10s of seconds, as shown in figure 12(b). The two significant implications from this discussion of performance are (1) that the overall performance of this device is low with thrust in the micronewton range and specific impulse levels little better than cold gas, and (2) the analytical model overpredicts the performance. This type of low performance is consistent with most low power magnetic nozzles to date [11, 14, 15]. We also emphasize that, although we show efficiency values in figure 8 on the order of 10%, these are only nozzle efficiencies. In practice, taking into consideration RF coupling and wall losses in the liner, the overall efficiency of this system is less than 1%, as is also consistent with most low power studies.

In either case, despite the low overall performance, one of the major findings from this work is that in low power operation analytical predictions that rest on ascribing the throat location simply to be coincident with the peak magnetic field are insufficient. The correct performance can only be recovered if the location of the throat is moved to the actual ion sonic line. We discuss in the next section a possible physical explanation for why this result occurs at low power.

5. Discussion

In this section, we examine potential physical mechanisms that may drive the shift in the location of the sonic point in the nozzle from the location of peak magnetic field intensity. Informed by our previous work [12], the hypotheses outlined in Correyero *et al* [16], and studies on these low temperature devices [3, 5, 7, 10, 24], the conjecture we explore here is that the throat may be driven downstream by collisional or ionization processes. In particular, this plasma has a low ionization fraction which results in a high neutral density within the nozzle exhaust, leading to effects not accounted for in an ideal analysis of magnetic nozzle performance. We look at three neutral-dependent mechanisms in particular: enhanced resistivity, charge exchange collisions, and ionization within the plume.

5.1. Electron-neutral collisions

In order for the nozzle to accelerate the ions up to sonic speed, the electrons must be influenced by the magnetic field. Sufficiently upstream of the throat and within the source the plasma is dominated by the neutral propellant gas. In this region electron-neutral collisions act to de-magnetize the electrons. At some point within the source tube in a sufficiently ionized device, the degree of ionization becomes high enough that neutral collisions no longer dominate and the plasma is guided by the converging-diverging magnetic field lines. However, we conjecture that due to the very low ionization fraction (~0.1%–1%) the plasma remains dominated by collisions in the near-field plume. This precludes the accelerating action of the magnetic field until the neutral gas becomes sufficiently sparse that the electrons become magnetized.

To evaluate this mechanism empirically, we consider the electron-neutral Hall parameter:

$$\Omega = \frac{qB}{m_e \nu_{en}}, \tag{8}$$

where B is the local magnetic field strength, m_e is the electron mass, and ν_{en} is the electron-neutral collision frequency. This electron-neutral collision frequency is calculated using the measured electron temperature and neutral density, and the cross section data outlined by Katz *et al* [58]. Physically, if the Hall parameter is large ($\Omega \gg 1$) an electron undergoes many gyrorotations between collisions with a neutral. Conversely, if the Hall parameter is small, an electron undergoes either partial or few gyrorotations between collisions with a neutral. During each collision with a neutral an electron can move to an adjacent nozzle streamline; a large collision frequency results in enhanced cross-field electron transport. This behavior is inconsistent with the idealized, collisionless models outlined above, suggesting that the models may not be suitable for predicting device performance.

Embedded within the electron-neutral collision frequency is a dependency on neutral density. In order to evaluate this parameter, we mapped the neutral density of the device. To this end, we show in figure 13 the neutral density as inferred

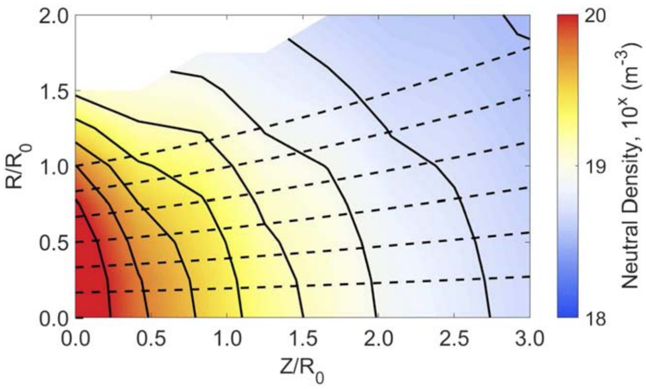

Figure 13. A spatial map of the neutral density (contour and solid black curves) with an overlay of the magnetic nozzle field lines (dashed black curves) for the 400 G, ~170 W net deposited power, and 3 mg s^{-1} xenon propellant flow rate source operating condition.

from pressure measurements made using a Stabil Ion Gauge with an integrated pitot tube. Note that the measurements are taken without power to the RF antenna, but the measured plasma density is typically ~3 orders of magnitude lower than the neutral density at the source exit plane. This low ion fraction suggests that the neutral profile shape does not significantly change with plasma ignition.

We show in figure 14 a comparison of the electron-neutral collision frequency with the local magnetic nozzle field strength via an electron Hall parameter analysis for three magnetic field settings. We also show on these plots a dotted line coincident with the experimentally determined sonic condition for the ions, i.e. the so-called sonic transition. Significantly, we see that with increasing magnetic field strength this line shifts further downstream and coincides with Hall parameter values of 70–200—values that are indicative of a magnetized electron fluid. Fundamentally, these plots show opposite trends between Hall parameter and the throat location; as the nozzle field strength increases the Hall parameter increases within the near-field while the ion sonic transition moves further downstream. For clarity, this trend is illustrated in figure 15, where the centerline Hall parameter is compared to the centerline ion Mach number. Physically, this trend states that as the magnetic field increases the electrons in the near-field plume are becoming more magnetized closer to the source exit plane. The fact that this trend is counter to the downstream movement of the throat suggests that, while electron de-magnetization may play a role in the delayed ion acceleration, it is likely not a dominant mechanism.

While electron-neutral collisions may not be a dominant mechanism to explain the downstream throat it is interesting to note that the electrons appear to be magnetized upstream of the ion sonic line. This is consistent with the analogy of a de Laval nozzle where the gas is accelerated through a converging section to sonic velocity—the electrons should be effectively magnetized at the sonic point. In keeping with this analogy the electrons must be magnetized for some extent upstream of the sonic line to be compressed and accelerated to the sonic condition at the throat; the Hall parameter values of 70–200 provides evidence that this criterion is met.

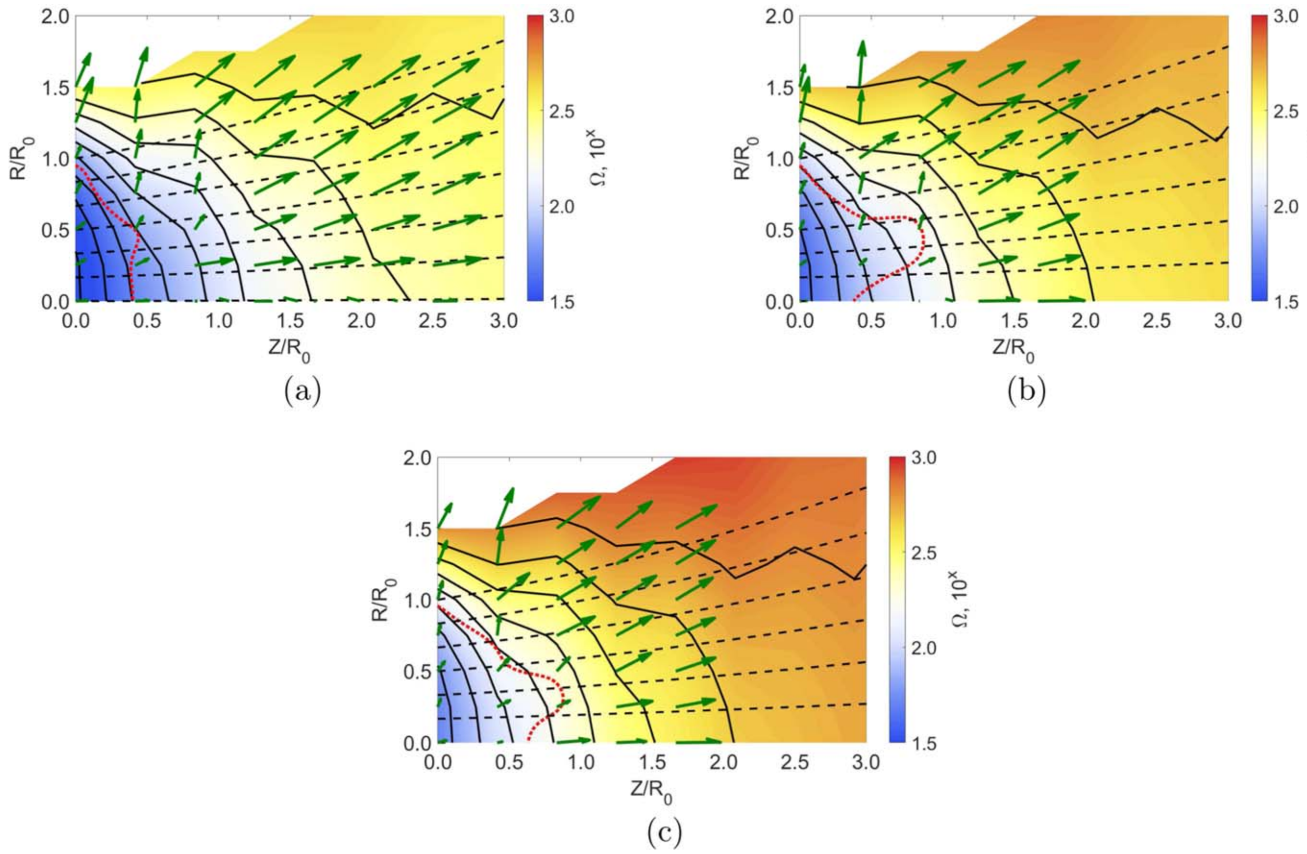

Figure 14. The electron-neutral Hall parameter (contour and solid curves) overlain with the magnetic nozzle (dashed curves) and ion sonic line (dotted curves) for the (a) 200 G, (b) 300 G, and (c) 400 G source operating condition. For all conditions the net deposited power is $\sim$170 W and the propellant flow rate is 3 mg s^{-1} xenon.

5.2. Ion-neutral collisions

A high density neutral population in the near-field region may also lead to frequent ion-neutral charge exchange collisions (CEX). These collisions act as a drag term on the ion fluid, preventing the ions from reaching sonic speeds until downstream of the high neutral pressure region, resulting in the throat shifting downstream into the plume. To assess the possible impact of this drag term the CEX mean free path (λ_{CEX}) can be compared to the characteristic length scale of ion acceleration. Since the ion acceleration appears to be governed by electrostatic acceleration (see section 4) the relevant characteristic length scale for acceleration can be written as $(-\nabla\phi/\phi)^{-1}$. The ratio of CEX mean free path to acceleration length is then $-\lambda_{\mathrm{CEX}}\nabla\phi/\phi$. If the CEX mean free path is shorter than the acceleration length scale ($-\lambda_{\mathrm{CEX}}\nabla\phi/\phi < 1$) the ions are experiencing a drag force through frequent CEX collisions. Conversely, if $-\lambda_{\mathrm{CEX}}\nabla\phi/\phi > 1$ the ion acceleration is not significantly impeded by these collisions. To quantify the role of CEX collisions within our low power test article we track the centerline evolution of this ratio across four magnetic field conditions (see figure 15). By tracking this parameter we see that as the magnetic field increases the axial location at which the CEX mean free path becomes equal to the acceleration length scale ($-\lambda_{\mathrm{CEX}}\nabla\phi/\phi = 1$) shifts downstream. This trend is influenced by two primary factors: (1) in our device, as the magnetic field increased the measured plasma density decreased. This trend is opposite of the improved confinement with increasing magnetic field observed in other magnetic nozzle devices [2, 5, 6, 10, 34, 44]. This deviation from the expected may be attributed to the quality of the plasma-antenna power coupling, which is shown by modeling results of similarly configured magnetically enhanced inductively coupled plasmas used in plasma processing applications to degrade when a critical magnetic field threshold is achieved [49, 50]. While the critical magnetic field is dependent on plasma species, source and antenna geometry, magnetic topology, and dominant power coupling mechanisms, it can drop into the 10–100 s of Gauss range [49, 50], which overlaps with our magnetic operating conditions. Estimation of the skin depth—a small region into which the bulk of the power is deposited—for these operating conditions show that the skin depth decreases from $\sim$1 cm to $\sim$1 mm with our increasing magnetic field conditions, further suggesting that this trend arises from the power coupling. This means that, with a constant propellant flow rate across all device operating conditions, this trend necessitates a corresponding slight increase in the un-ionized neutral density in the near-field with increasing magnetic field. This acts to decrease the CEX mean free path. (2) As the magnetic field increased we observed a decrease in the overall potential drop from source

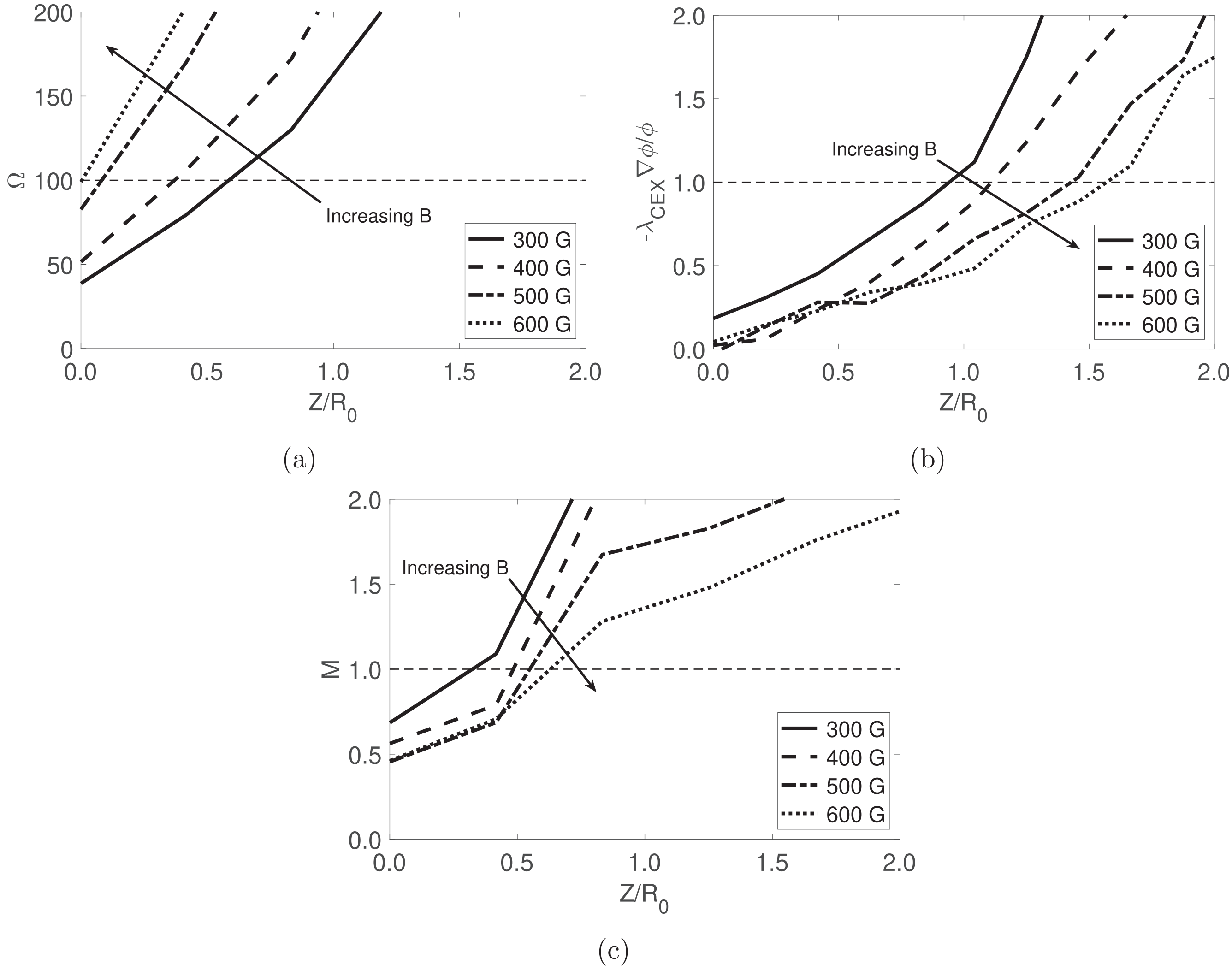

Figure 15. The centerline evolution of the (a) electron-neutral Hall parameter, (b) the ratio of the charge exchange mean free path and characteristic ion acceleration length scale, and (c) the ion Mach number for the 300–600 G operating conditions. For all operating conditions the net deposited power is ~170 W and propellant flow rate is 3 mg s^{-1} xenon.

exit plane to the nozzle detachment plane. This acts to increase the characteristic acceleration length. Both of these effects act to shift the location of $-\lambda_{\mathrm{CEX}}\nabla\phi/\phi = 1$ downstream. Significantly, this trend in $-\lambda_{\mathrm{CEX}}\nabla\phi/\phi$ qualitatively matches the downstream movement of the ion sonic transition line with increasing magnetic field. This correlational evidence suggests that ion-neutral CEX collisions may play an important role in shifting the effective nozzle throat downstream. The collision-induced drag on the ions may delay the acceleration of the subsonic ions, resulting in the sonic condition being met at the downstream throat location.

5.3. Ionization within the plume

In addition to the collisional processes discussed above, ionization may also play a role in pushing the ion sonic line downstream. The volumetric rate of ionization within the near-field plume region can be estimated from a control volume continuity analysis. Leveraging axisymmetry, assuming steady flow, and bounding the control volume to the region with LIF measurements (refer to figure 6), this takes the form

$$K_{iz,p} = \frac{2\pi\Gamma_r R\ell + \pi\Gamma_a R^2 - \pi\Gamma_0 R_0^2}{\pi\bar{n}_g\bar{n}_e R^2\ell}, \tag{9}$$

where R is the radius of the cylindrical control volume, ℓ is the length of the control volume, and Γ_r, Γ_a, and Γ_0 are the particle fluxes through the radial, axial, and source exit plane boundaries, respectively. This volumetric ionization rate can be compared to the estimated ionization rate within the source tube—the location where the RF power is intended to be applied to the propellant. As shown in figure 16, in the magnetic field conditions that exhibit a downstream throat the volumetric ionization rate within the near-field plume region is 15%–35% of the ionization rate within the source tube. This indicates that the RF power may be leaking into the near-field plume region or Ohmic heating may be causing significant ionization. This behavior is consistent with numerical

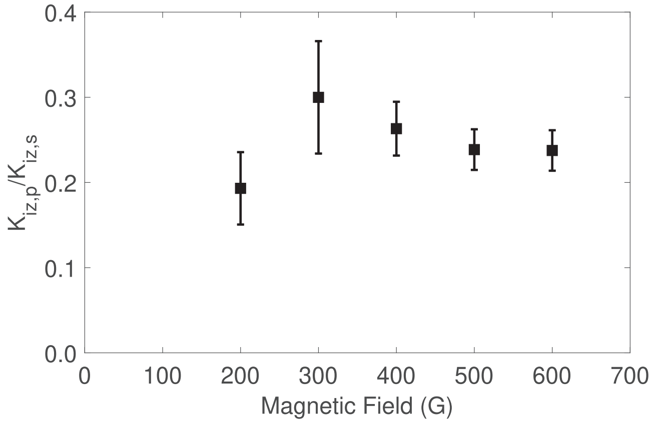

(a)

Figure 16. The ratio of the volumetric ionization rate in the near-field plume region (as bounded by the LIF measurements) and the volumetric ionization rate within the source region. For all magnetic field conditions the net deposited power is ∼170 W and propellant flow rate is 3 mg s^{-1} xenon.

results for magnetically enhanced inductively coupled plasma processing units—devices with similar power coupling architectures and magnetic topographies—that also predict power coupling downstream of the primary ionization and heating region [49, 50]. This result is also consistent with particle-in-cell modeling results of a plasma thruster plume by Li *et al* [59], who show that a significant fraction of the input power may leak into the thruster plume. While there is no clear trend in ionization rate within the plume compared to the magnetic field operating condition, the source conditions in which we observe a downstream effective throat location exhibit significant levels of ionization. This correlation suggests that it may play an important role in the near-field region, and, subsequently, the ion acceleration in that region. The ions that are born in the near-field plume region fall through a smaller potential drop than the ions born in the source tube—except, possibly, those ions that have undergone CEX collisions. This newly-ionized population may significantly reduce the mean ion speed within the fluid, thereby acting as an effective drag term on the ions. This ionization-induced drag description is consistent with the findings of Hooper, in a similar device architecture [60].

The ultimate implication from the above discussion is that the low ionization fraction and corresponding high neutral density seems like a plausible explanation for the movement in the effective throat of the magnetic nozzle. This is evidence in support of the idea that modeling treatments of these systems at low power must be more nuanced, taking into consideration more than singly-charged, fully-ionized plasma. With that said, we recognize that three processes discussed here may not be the only or dominant driving factors, and their interactions with the plume expansion may vary between devices. Other near-field detachment processes have been recently identified [13] which may also have an effect here. The relationships we see, particularly with the charge exchange process, are compelling but correlational at this point.

6. Conclusions

In summary, the 2D plasma properties of an experimental low power magnetic nozzle plasma source operating at various magnetic fields have been measured using electrostatic probes and LIF. In all of the operating conditions a high neutral density region is observed in the near-field. The ions initially leave the source region subsonically and the axial ion acceleration region is pushed downstream in high magnetic field cases. The impact of this downstream movement of the throat on thrust performance is estimated using spatial plasma property maps to predict the thrust and specific impulse performance of the source. The measurement-inferred performance is compared to the expected performance of an ideal, fully attached nozzle operating at the same conditions; the performance of the low power device is ∼50%–70% of the ideal performance. This measured performance deficit is attributed to the reduced ion acceleration due to the effective shortening of the magnetic nozzle and the throat being pushed downstream. By adjusting the model initial conditions to match the empirical downstream throat properties the predicted performance agrees with the results inferred from plume measurements. This finding is consistent with the recent work performed by Correyero *et al* [16], though for a low power ECR source compared to our low power inductive source.

Three potential mechanisms that drive the ion sonic transition downstream are explored: electron-neutral collisions, ion-neutral collisions, and ionization within the plume. The electron-neutral collision mechanism is evaluated using a Hall parameter analysis. This analysis indicates that the electrons become more magnetized closer to the source exit plane as the magnetic field strength increases. This runs counter to the measurement-inferred trend of the effective nozzle throat moving further downstream with increasing magnetic field, suggesting that this mechanism may not be directly responsible for the shift in the throat location. The impact of ion-neutral collisions, effectively a drag term on the ion fluid, is explored by comparing the CEX mean free path to the characteristic electrostatic acceleration length scale. On device centerline the trend in the downstream movement of the throat location and this parameter are positively correlated, suggesting that this mechanism plays an important role in the near-field expansion and ion acceleration. Finally, in the magnetic field cases that exhibit a downstream throat the volumetric ionization rate in the near-field plume region is estimated to be 15%–35% of the ionization rate within the source. This presence of ionization within the plume is correlated with the downstream shift in the effective nozzle throat. This suggests that ionization in the near-field may also play a role in the plasma-nozzle interaction. Overall, it is observed that in a low power magnetic nozzle test article a mechanism exists that shifts the nozzle throat downstream, effectively reducing thrust performance compared to ideal model predictions. As the research and development trends in the field shift toward developing low power versions of these devices, this finding suggests that it is necessary to include these low-ionization fraction effects in future models and iterations of these devices.

Acknowledgments

This research has been reproduced from [61]. This material is based upon work supported by the National Science Foundation Graduate Research Fellowship Program under Grant No. DGE 1256260. The authors would like to acknowledge the members of the Plasmadynamics and Electric Propulsion Laboratory for their insightful discussion concerning this research.

Appendix

When evaluating the denominator of (2), the power entering the nozzle is modeled as the sum of the power stored in the flowing ions, in the plasma pressure, and the electron heat conduction. Assuming the plasma profiles are axisymmetric at each axial slice of the nozzle, the power stored within the flowing ions can be inferred from plasma measurements using

$$P_v = \int_0^{R_s} \pi m_i n u_{\text{ion}}^3 r \mathrm{d}r, \tag{A.1}$$

where m_i is the ion mass, n is the plasma density, r is the radial coordinate, and R_s is the source tube radius at the exit plane. The power stored within the plasma pressure is

$$P_p = \int_0^{R_s} 5\pi q n T_e u_{\text{ion}} r \mathrm{d}r. \tag{A.2}$$

Assuming that the plasma within the plume is globally governed by polytropic cooling the heat conduction term [39] can be written as

$$P_Q = \int_0^{R_s} 3\pi q n T_e u_{\text{ion}} \left(\frac{5/3 - \gamma}{\gamma - 1}\right) r \mathrm{d}r. \tag{A.3}$$

Physically, this is the energy flowing through the electron fluid along the nozzle field lines to maintain the plasma gradients present within the plume.

The power consumed in creating the ions can be accounted for by

$$P_c = \int_0^{R_s} 2\pi q n \epsilon_c u_{\text{ion}} r \mathrm{d}r, \tag{A.4}$$

where ϵ_c is the ion cost in eV. The ion cost can be interpreted as the net energy required to create an ion-electron pair. As demonstrated in the analysis of ion cost presented by Lieberman and Lichtenberg [56]:

$$K_{iz}(T_e)\epsilon_c = K_{iz}(T_e)\epsilon_{iz} + \sum_{j=1}^{\infty} K_{\text{exc},j}(T_e)\epsilon_{\text{exc},j} + \frac{3m_e}{m_i} K_{el} T_e; \tag{A.5}$$

the ion cost exceeds the ionization energy due to the presence of excited states that absorb a portion of the energy. Note that in the above expression K_{iz} is the volumetric ionization rate, K_{exc} is the volumetric excitation rate, K_{el} is the volumetric polarization scattering rate, ϵ_{iz} is the ionization energy, ϵ_{exc} is the excitation energy, and j is the state index. Both the ionization and excitation rates are functions of electron temperature. Note that the ion cost exceeds the ionization energy due to the presence of excited states and collisions with neutrals that absorb a portion of the absorbed energy. This expression captures the electron energy loss due to the dominant loss mechanisms for weakly ionized monatomic electropositive plasmas [56].

The power entering the nozzle is then the sum of (A.1)–(A.4), or

$$P_{\text{noz}} = P_v + P_p + P_Q + P_c. \tag{A.6}$$

ORCID iDs

T A Collard https://orcid.org/0000-0002-0723-4868
B A Jorns https://orcid.org/0000-0001-9296-2044

References

[1] Takahashi K, Lafleur T, Charles C, Alexander P, Boswell R W, Perren M, Laine R, Pottinger S, Lappas V and Harle T 2011 Direct thrust measurement of a permanent magnet helicon double layer thruster *Appl. Phys. Lett.* **98** 141503
[2] Takahashi K, Charles C, Boswell R W and Ando A 2013 Performance improvement of a permanent magnet helicon plasma thruster *J. Phys. D: Appl. Phys.* **46** 352001
[3] Merino M and Ahedo E 2014 Plasma detachment in a propulsive magnetic nozzle via ion demagnetization *Plasma Sources Sci. Technol.* **23** 032001
[4] Ahedo E and Merino M 2011 On plasma detachment in propulsive magnetic nozzles *Phys. Plasmas* **18** 053504
[5] Ahedo E and Merino M 2012 Two-dimensional plasma expansion in a magnetic nozzle: separation due to electron inertia *Phys. Plasmas* **19** 083501
[6] Ahedo E and Merino M 2010 Two-dimensional supersonic plasma acceleration in a magnetic nozzle *Phys. Plasmas* **17** 073501
[7] Ahedo E and Navarro-Cavalle J 2013 Helicon thruster plasma modeling: Two-dimensional fluid-dynamics and propulsive performances *Phys. Plasmas* **20** 043512
[8] Fruchtman A, Takahashi K, Charles C and Boswell R W 2012 A magnetic nozzle calculation of the force on a plasma *Phys. Plasmas* **19** 033507
[9] Lafleur T, Cannat F, Jarrige J, Elias P Q and Packan D 2015 Electron dynamics and ion acceleration in expanding-plasma thrusters *Plasma Sources Sci. Technol.* **24** 065013
[10] Lafleur T 2014 Helicon plasma thruster discharge model *Phys. Plasmas* **21** 043507
[11] Vialis T, Jarrige J and Packan D 2017 Geometry optimization and effect of gas propellant in an electron cyclotron resonance plasma thruster *35th Int. Electric Propulsion Conf. (Atlanta, GA)*
[12] Collard T A, Byrne M P, Hepner S T, Durot C J and Jorns B A 2017 Investigation of detachment in a miniature magnetic nozzle source *35th Int. Electric Propulsion Conf. (Atlanta, GA)*
[13] Hepner S T, Wachs B N, Collard T A and Jorns B A 2018 Observation of low frequency plasma oscillations in the

plume of a partially magnetized magnetic nozzle *54th AIAA/SAE/ASEE Joint Propulsion Conf. AIAA Propulsion and Energy Forum* (American Institute of Aeronautics and Astronautics)
[14] Siddiqui M U and Cretel C 2018 Updated performance measurements and analysis of the phase four RF thruster *AIAA Propulsion and Energy Forum* (American Institute of Aeronauticsand Astronautics)
[15] Siddiqui M U, Cretel C, Synowiec J, Hsu A G, Young J A and Specktor R 2017 First performance measurements of the phase four rf thruster *Proc. 35th IEPC (Atlanta, USA)* IEPC-2017-431
[16] Correyero S, Jarrige J, Packan D and Ahedo E 2018 Ion acceleration in the magnetic nozzle of an ECR thruster: Comparison of experimental measurements with a quasi 1D kinetic model *2018 Space Propulsion Conf.*
[17] Martinez-Sanchez M and Pollard J E 1998 Spacecraft electric propulsion—an overview *J. Propul. Power* **14** 688–99
[18] Grondein P, Lafleur T, Chabert P and Aanesland A 2016 Global model of an iodine gridded plasma thruster *Phys. Plasmas* **23** 033514
[19] Szabo J, Pote B, Paintal S, Robin M, Hillier A, Branam R D and Huffmann R E 2012 Performance evaluation of an iodine-vapor Hall thruster *J. Propul. Power* **28** 848–57
[20] Szabo J, Robin M, Paintal S, Pote B, Hruby V and Freeman C 2013 Iodine propellant space propulsion *Proc. 33rd Int. Electric Propulsion Conf.* pp 2013–311
[21] Polzin K A and Peeples S 2014 Iodine Hall thruster propellant feed system for a cubesat *50th Joint Propulsion Conf. (Cleveland, OH)*
[22] Tverdokhlebov O S and Semenkin A V 2001 Iodine propellant for electric propulsion to be or not to be *7th IAA/ASME/SAE/ASEE Joint Propul. Conf. Exhib. (Salt Lake City, UT)* (https://doi.org/10.2514/6.2001-3350)
[23] Hofer R R, Goebel D M, Mikellides I G and Katz I 2014 Magnetic shielding of a laboratory Hall thruster: II. Experiments *J. Appl. Phys.* **115** 043304
[24] Little J M and Choueiri E Y 2013 Thrust and efficiency model for electron-driven magnetic nozzles *Phys. Plasmas* **20** 103501
[25] Takahashi K, Akahoshi H, Charles C, Boswell R W and Ando A 2017 High temperature electrons exhausted from rf plasma sources along a magnetic nozzle *Phys. Plasmas* **24** 084503
[26] Bouwmeester J and Guo J 2010 Survey of worldwide pico-and nanosatellite missions, distributions and subsystem technology *Acta Astronaut.* **67** 854–62
[27] Takahashi K, Chiba A, Komuro A and Ando A 2016 Experimental identification of an azimuthal current in a magnetic nozzle of a radiofrequency plasma thruster *Plasma Sources Sci. Technol.* **25** 055011
[28] Takahashi K, Lafleur T, Charles C, Alexander P and Boswell R W 2011 Electron diamagnetic effect on axial force in an expanding plasma: experiments and theory *Phys. Rev. Lett.* **107** 235001
[29] Seikel G R 1962 Generation of thrust-electromagnetic thrustors *Electric Propulsion for Spacecraft* (*NASA Special Publication* vol 22) (Washington: NASA) pp 19
[30] Arefiev A V and Breizman B N 2005 Magnetohydrodynamic scenario of plasma detachment in a magnetic nozzle *Phys. Plasmas* **12** 043504
[31] Hooper E B 1993 Plasma detachment from a magnetic nozzle *J. Propul. Power* **9** 757–63
[32] Moses R W, Gerwin R A and Schoenberg K F 1992 Resistive plasma detachment in nozzle based coaxial thrusters *AIP Conf. Proc.* **246** 1293–303
[33] Cohen S A and Paluszek M A 1998 The grand challenge—a new plasma thruster *Launchspace* **3** 46–50
[34] Little J M 2015 Performance scaling of magnetic nozzles for electric propulsion *PhD Thesis* Princeton University
[35] Andersen S A, Jensen V O, Nielsen P and D'Angelo N 1969 Continuous supersonic plasma wind tunnel *Phys. Fluids* **12** 557–60
[36] Hill P G and Peterson C R 1992 *Mechanics and thermodynamics of propulsion* (2nd Revised and Enlarged edition) (Reading, MA: Addison-Wesley Publishing Co.)
[37] Goebel D M and Katz I 2008 *Fundamentals of Electric Propulsion: Ion and Hall Thrusters* vol 1 (New York: Wiley)
[38] Fruchtman A 2011 The thrust of a collisional-plasma source *IEEE Trans. Plasma Sci.* **39** 530–9
[39] Merino M and Ahedo E 2015 Influence of electron and ion thermodynamics on the magnetic nozzle plasma expansion *IEEE Trans. Plasma Sci.* **43** 244–51
[40] Little J M and Choueiri E Y 2016 Electron cooling in a magnetically expanding plasma *Phys. Rev. Lett.* **117** 225003
[41] Deline C A, Bengtson R D, Breizman B N, Tushentsov M R, Jones J E, Chavers D G, Dobson C C and Schuettpelz B M 2009 Plume detachment from a magnetic nozzle *Phys. Plasmas* **16** 033502
[42] Dannenmayer K and Mazouffre S 2013 Electron flow properties in the far-field plume of a Hall thruster *Plasma Sources Sci. Technol.* **22** 035004
[43] Zhang Z, Tang H, Kong M, Zhang Z and Ren J 2015 Electron temperature Measurement in Maxwellian non-isothermal beam plasma of an ion thruster *Rev. Sci. Instrum.* **86** 023506
[44] Lafleur T, Takahashi K, Charles C and Boswell R W 2011 Direct thrust measurements and modelling of a radio-frequency expanding plasma thruster *Phys. Plasmas* **18** 080701
[45] Durot C J, Gallimore A D and Smith T B 2014 Validation and evaluation of a novel time-resolved Laser-induced fluorescence technique *Rev. Sci. Instrum.* **85** 013508
[46] Sheridan T E 2000 How big is a small Langmuir probe? *Phys. Plasmas* **7** 3084–8
[47] Sheehan J P and Hershkowitz N 2011 Emissive probes *Plasma Sources Sci. Technol.* **20** 063001
[48] Brockhaus A, Borchardt C and Engemann J 1994 Langmuir probe measurements in commercial plasma plants *Plasma Sources Sci. Technol.* **3** 539
[49] Kinder R L and Kushner M J 2001 Wave propagation and power deposition in magnetically enhanced inductively coupled and helicon plasma sources *J. Vac. Sci. Technol.* A **19** 76–86
[50] Kinder R L and Kushner M J 2001 Noncollisional heating and electron energy distributions in magnetically enhanced inductively coupled and helicon plasma sources *J. Appl. Phys.* **90** 3699–712
[51] Bamford R *et al* 2008 The interaction of a flowing plasma with a dipole magnetic field: measurements and modelling of a diamagnetic cavity relevant to spacecraft protection *Plasma Phys. Control. Fusion* **50** 124025
[52] Tsui H Y W *et al* 1993 A comparison of edge turbulence in tokamaks, stellarators, and reversed-field pinches *Phys. Fluids* B **5** 2491–7
[53] Antoni V, Desideri D, Martines E, Serianni G and Tramontin L 1997 Plasma potential well and velocity shear layer at the edge of reversed field pinch plasmas *Phys. Rev. Lett.* **79** 4814–7 PRL
[54] Jorns B, Dodson C A, Anderson J R, Goebel D M, Hofer R R, Sekerak M J, Lopez Ortega A and Mikellides I G 2016 Mechanisms for pole piece erosion in a 6-kW magnetically-shielded Hall thruster *AIAA Propulsion and Energy Forum* (American Institute of Aeronautics and Astronautics) (https://doi.org/10.2514/6.2016-4839)
[55] Huang W, Gallimore A D and Hofer R R 2011 Neutral flow evolution in a six-kilowatt Hall thruster *J. Propul. Power* **27** 553–63

[56] Lieberman M A and Lichtenberg A J 1994 Principles of plasma discharges and materials processing *MRS Bull.* **30** 899–901

[57] Brown D L, Walker M L R, Szabo J, Huang W and Foster J E 2016 Recommended practice for use of Faraday probes in electric propulsion testing *J. Propul. Power* **33** 3

[58] Katz I, Anderson J R, Polk J E and Brophy J R 2003 One-dimensional hollow cathode model *J. Propul. Power* **19** 595–600

[59] Li M, Merino M, Ahedo E and Tang H 2019 On electron boundary conditions in PIC plasma thruster plume simulations *Plasma Sources Sci. Technol.* **28** 034004

[60] Hooper E B Jr 1995 Plasma flow resulting from electron cyclotron resonance heating on a magnetic hill *Phys. Plasmas* **2** 4563–9

[61] Collard T A 2019 Performance characterization of a low power magnetic nozzle *PhD thesis* University of Michigan